Chapter 4

Non-Gaussianity Detections Using Spherical Mexican Hat Wavelets

4.1 The Wavelets on 2-Sphere

It has been well known that the discrete wavelet transform (DWT) defined on the plane is a versatile tool in image processing and the CMB analysis can be viewed as a task in this field. For this reason, the 2-D DWT was applied to the CMB data in the early works of investigations for non-Gaussian signature using wavelet analysis. Beside that, the early CMB data lie on a small patch of the sky in which the Euclidean limit works. There have just been two releases of the all-sky data: the CMB data from NASA's COsmic Background Explorer (COBE) satellite (the data are available since 1992) and from NASA's Wilkinson Microwave Probe (WMAP) (available since 2003). The all-sky data from the Planck satellite of the European Space Agency (ESA) is expected to be available in 2007. Indeed, the data from COBE are projected on six faces of the cube by the Quad-Cube pixelization. Hence, the first non-Gaussianity investigation using wavelets performed on the COBE data applied a DWT defined on the plane [21]. However, there is currently the pixelization scheme onto the sphere, called HEALPix [22], and the COBE data has been re-analyzed by using the spherical wavelets, namely the spherical Haar wavelets [23] and the spherical Mexican hat wavelets [24].

As suggested in Martinez-Gonzalez et al. [25], the HEALPix pixelization provides less biases than the Quad-Cube pixelization so that it is better to perform the wavelet analysis on the all-sky data pixelized onto the sphere. The HEALPix pixelization which possesses the equal area iso-latitude pixels introduce the biases since the distances between one pixel and its neighbours vary with latitude; pixels near the equator tend to be more uniformly distributed than those near the poles. The biases from this cause can be reduced by using the continuous wavelet transform because it averages over many pixels. Hence, we are interested in the spherical continuous wavelet transform like the spherical Mexican hat wavelet transform which is an isotropic wavelet.

The stereographic projection on the sphere is an appropriate way to construct a spherical continuous wavelet transform from the plane wavelet with the properties required for a *genuine* continuous wavelet transform on the sphere[1], it is based on the group theory approach proposed by Antoine and Vanderghenst 1998 [26]. The stereographic projection $(\mathbf{x} = (x_1, x_2)) \mapsto (\theta, \phi)$ provides the relations (see Fig. 4.1)

$$x_1 = 2\tan\frac{\theta}{2}\cos\phi, \quad x_2 = 2\tan\frac{\theta}{2}\sin\phi, \tag{4.1}$$

where (θ, ϕ) are the polar coordinates on the sphere, and then the polar coordinates in the tangent plane to the North pole are $(2\tan\frac{\theta}{2}, \phi)$.

For the isotropic wavelet $\Psi(x; R)$, where $x = |\mathbf{x}|$, its extension to the sphere is

$$\Psi_S(\theta; R) \propto \left(\cos\frac{\theta}{2}\right)^{-4} \Psi(x \equiv 2\tan\frac{\theta}{2}; R) \quad , \tag{4.2}$$

which incorporates the basic properties:

(a) the compensation: $\int \mathrm{d}\theta \mathrm{d}\phi \sin\theta \Psi_S(\theta; R) = 0$,

(b) the translations along the sphere which is given by the rotations from $SO(3)$,

---

[1] The following properties are required to obtain a genuine CWT on the sphere [26]:

- the signals and wavelets must live on the sphere;
- the transform must involve (local) dilations of some kind; and
- possibly the CWT on S^2 should reduce locally to the usual CWT on the (tangent) plane (Euclidean limit).

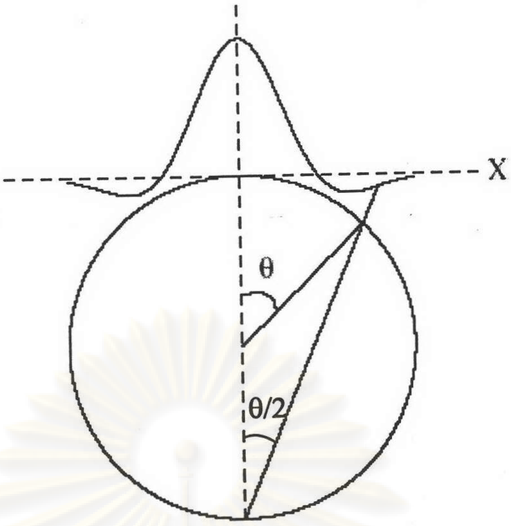

Figure 4.1: The stereographic projection from the plane to unit sphere of the Mexican hat wavelet [25].

(c) the local dilations on the sphere which can be obtained by the stereographic projection of the dilations on the tangent plane, and

(d) the wavelet on S^2 is recovered to the wavelet on the plane for small angles (Euclidean limit).

Note that the stereographic projection preserves the properties of the two dimensional CWT as indicated in (a), (b) and (c), and (d) is the property that usually belongs to any object defined on the spherical geometry.

Similar to the two dimensional CWT, the spherical continuous wavelet transform has the strategy for the analysis and synthesis (or reconstruction) as follows:

- **Analysis**

  For a function on the sphere $f(\theta, \phi)$, the linear transform with respect to the spherical continuous wavelets $\Psi_S(\theta; R)$ derived from the inverse stereographic projection is

$$\tilde{w}(\mathbf{x}, R) = \int \mathrm{d}\theta' \mathrm{d}\phi' \sin\theta' \, \tilde{f}(\mathbf{x} + \mathbf{\Lambda}) \Psi_S(\theta'; R), \tag{4.3}$$

  where $\mathbf{x} \equiv 2\tan\frac{\theta}{2}(\cos\phi, \sin\phi)$, $\mathbf{\Lambda} \equiv 2\tan\frac{\theta'}{2}(\cos\phi', \sin\phi')$, $\tilde{f}(\mathbf{x}) \equiv f(\theta, \phi)$, and $\tilde{w}(\mathbf{x}, R) \equiv w(\theta, \phi; R)$. Note that the spherical continuous wavelet transformation transforms from a sphere defined by the polar coordinates (θ, ϕ) to the multi-scale spherical space defined by the coordinates (θ, ϕ, R).

- **Synthesis**

  We can reconstruct the function $f(\theta, \phi)$ from the wavelet coefficients $w(\theta, \phi; R)$ by using the formula:

$$f(\theta, \phi) \equiv \tilde{f}(\mathbf{x}) = \frac{1}{C_\psi} \int \mathrm{d}\theta' \mathrm{d}\phi' \, \sin\theta' \, \frac{\mathrm{d}R}{R^3} \, \tilde{w}(\mathbf{x} + \mathbf{\Lambda}, R) \Psi_S(\theta'; R), \qquad (4.4)$$

  where $\tilde{w}(\mathbf{x}, R) \equiv w(\theta, \phi; R)$.

4.2 The Spherical Mexican Hat wavelets

The Mexican hat (MEXHAT) wavelet, which is a planar isotropic continuous wavelet, is defined by

$$\Psi(x; R) \equiv \Psi(\mathbf{x}; \mathbf{0}, R) = \frac{1}{(2\pi)^{1/2} R} \left[2 - \left(\frac{x}{R} \right)^2 \right] e^{-x^2/2R^2}, \qquad (4.5)$$

where $x = |\mathbf{x}|$. Note that this wavelet is proportional to the 2D Laplacian of the Gaussian function. It has been applied to detect the point sources in CMB.

The spherical Mexican hat wavelet (SMHW) can be obtained from the stereographic projection on the sphere of the Mexican hat wavelet. From Eq. (4.2), we have the SMHW defined by

$$\Psi_S(\theta; R) = \frac{1}{(2\pi)^{1/2} N(R)} \left[1 + \left(\frac{y}{2} \right)^2 \right]^2 \left[2 - \left(\frac{y}{R} \right)^2 \right] e^{-y^2/R^2}; \qquad (4.6)$$

$$N(R) \equiv \left(1 + \frac{R^2}{2} + \frac{R^4}{4} \right)^{1/2}, \quad y = 2 \tan \frac{\theta}{2}. \qquad (4.7)$$

Notice that $N(R)$ is the normalization constant that makes

$$\int \mathrm{d}\theta \mathrm{d}\phi \, \sin\theta \, \Psi_S^2(\theta; R) = 1 \qquad (4.8)$$

so that the transformation is unitary, and $\left[1 + \left(\frac{y}{2} \right)^2 \right]^2 = \left(\cos \frac{\theta}{2} \right)^{-4}$ which is introduced in Eq. (4.2). Fig. 4.2 shows the SMHW that is deformed from the Mexican hat wavelet. The analysis and synthesis with respect to this kind of wavelet follow Eqs. (4.3) and (4.4), respectively.

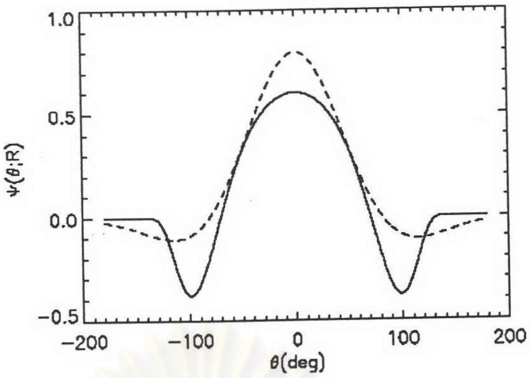

Figure 4.2: The spherical Mexican hat wavelet (SMHW) (solid line) deformed from the Mexican hat wavelet (dash line). The scale of the wavelet is chosen to be $R = 1$ rad [25].

4.3 The WMAP 1-year Data

In this thesis, we review the non-Gaussianity detections on the WMAP first year data using the spherical wavelet analysis according to Vielva et al. 2004 [27] (V04, from now on) and Mukherjee and Wang 2004 [28] (MW04, from now on). The results from WMAP are the full sky maps of data in 5 frequency bands: K-Band (22.8 GHz, 1 receiver), Ka-Band (33.0 GHz, 1 receiver), Q-Band (40.7 GHz, 2 receivers), V-Band(60.8 GHz, 2 receivers) and W-Band (93.5 GHz, 4 receivers).[2] Since only the data in Q-Band, V-Band and W-Band are dominated by CMB over the Galactic emission, the WMAP team for non-Gaussianity tests [29] suggested to use a noise-weighted sum of maps in these three frequency bands (8 receivers) in order that the signal-to-noise ratio increases. However, it is better to use the foreground cleaned maps from these 8 receivers, where the method of foreground cleaning is described in Bennett et al. 2003 [30], in this action to obtain better signal-to-noise ratio. The data analyzed by V04 and MW04 follow this choice of the combined map.

According to V04, the temperature $\hat{T}(\mathbf{x})$ on this Q-V-W coadded map where the maps of each frequency have already been foreground cleaned can be given

---

[2] See http://map.gsfc.nasa.gov or http://lambda.gsfc.nasa.gov

by[3] [30]

$$\hat{T}(\mathbf{x}) = \sum_{j=3}^{10} \hat{T}_j(\mathbf{x})\, w_j(\mathbf{x}), \tag{4.9}$$

where the indices $j = 3, 4$ refer to the Q-Band receivers, $j = 5, 6$ to the ones of the V-Band and $j = 7, 8, 9, 10$ to the receivers of the W-Band (the indices $j = 1, 2$ refer to the K and Ka receivers, respectively), and $w_j(\mathbf{x})$ is defined by

$$w_j(\mathbf{x}) = \frac{\bar{w}_j(\mathbf{x})}{\sum_{j=3}^{10} \bar{w}_j(\mathbf{x})}, \quad \bar{w}_j(\mathbf{x}) = \frac{N_j(\mathbf{x})}{\sigma_{0j}^2}, \tag{4.10}$$

where σ_{0j} is the noise dispersion per observation and $N_j(\mathbf{x})$ is the number of observations of the receiver j at position $\mathbf{x}$. This map is created in the Hierarchical, Equal Area and iso-Latitude Pixelization (HEALPix) [22] with the resolution $N_{side} = 512$ (about 13 arcminute FWHM), with the total number of pixels of $12 \times N_{side}^2 = 3,145,728$. Then the map is degraded to the map with resolution $N_{side} = 256$, $12 \times N_{side}^2 = 1,572,864$, since the very small scales are dominated by noise [27]. In addition, since the Galactic emission is strong at the Galactic plane and there are still the contaminations from known radio point sources, the mask Kp0 (available in LAMBDA site) which covers these regions is applied. Within the mask, the data are set to zero. When the Kp0 mask is applied, 76.8 % of the sky survives. Finally, the monopole and dipole outside the mask are removed. Then this is the map for the SMHW analysis (see Fig. 4.3).

4.4 Gaussian Simulations

A large number of simulations of Gaussian CMB maps is required for specifying the statistical significance of the test. The 10000 simulations were produced in V04 and 1000 simulations were produced in MW04. An estimator, such as skewness and kurtosis on each wavelet scale, is measured in every simulation. If we think of each simulation as an element of the ensemble of Gaussian maps, the estimator measured in different simulations can have different values around a particular value. The histogram obtained by collecting the values of the estimator from

---

[3] The foreground cleaned maps in each frequency band are available in the *Legacy Archive for Microwave Background Data Analysis* (LAMBDA) web page: http://lambda.gsfc.nasa.gov

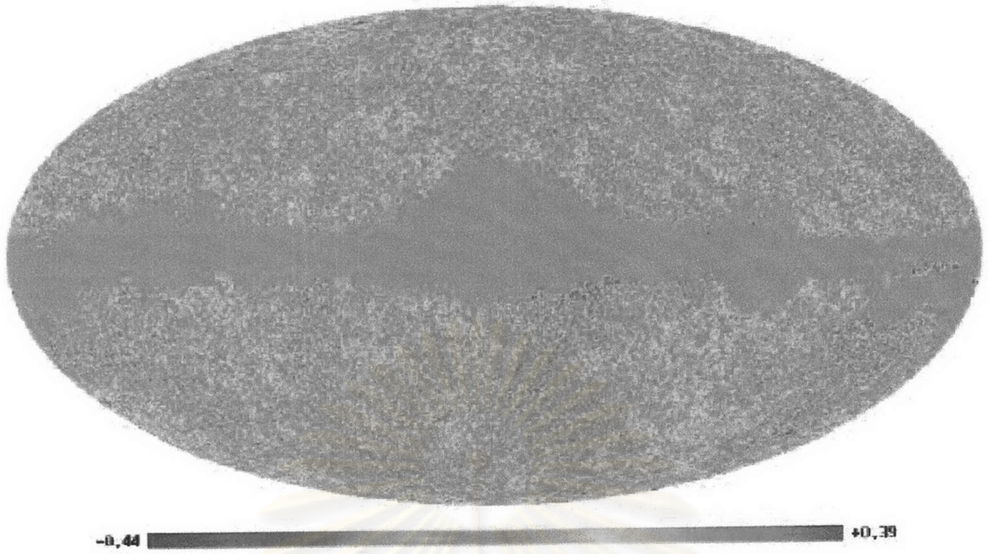

Figure 4.3: The (foreground cleaned) Q-V-W coadded map applied by the Kp0 mask with the resolution $N_{side} = 256$. The residual monopole and dipole have been removed. This figure is taken from V04 [27].

large numbers of simulations can represent the probability of getting the value of the estimator for the Gaussian case.

The Gaussian CMB realizations with the power spectrum C_l that best fits the WMAP 1st year data can be produced . Random Gaussian multipole coefficients a_{lm} of the temperature maps are generated and copied for each receiver. Then they are convolved with the Gaussian beams (available in LAMBDA site), where the sizes of the beams depend on the frequency bands, to get the resolution compatible with the experiment, here WMAP. After that, transform them from harmonic to real space, and add uncorrelated Gaussian noise realizations. Now we have the maps for all receivers corresponding to foreground cleaned maps for all receivers in the last section. Then we combine all maps using noise weight following Eq. (4.9). Finally, the 1000 simulations are degraded to $N_{side} = 256$, the $Kp0$ mask is applied, and the monopole and dipoles are removed for each simulation.

4.5 Statistical Analysis in Wavelet Space

To perform statistical analysis in wavelet coefficient space, the WMAP data and the Gaussian simulations are convolved with the SMHW at different scales, following the analysis formula in Eq. (4.3). In their works, the following scales of wavelets in arcmin unit are chosen: $R_1 = 13.7$ (0.23^o), $R_2 = 25$ (0.42^o), $R_3 = 50$ (0.83^o), $R_4 = 75$ (1.25^o), $R_5 = 100$ (1.67^o), $R_6 = 150$ (2.5^o), $R_7 = 200$ (3.33^o), $R_8 = 250$ (4.17^o), $R_9 = 300$ (5^o), $R_{10} = 400$ (6.67^o), $R_{11} = 500$ (8.33^o), $R_{12} = 600$ (10^o), $R_{13} = 750$ (12.5^o), $R_{14} = 900$ (15^o) and $R_{15} = 1050$ (17.5^o). It is important to emphasize that the wavelet scale is not really the angular scale in the sky. It is only the scale of the support of wavelets, which is defined on the Euclidean plane and then inverse stereographically projected onto the sphere. However, it is related to the angular scale in the sky. On these chosen scales, the angular scale in the sky is around 2 times the wavelet scale. That is the wavelet scales R_1 to R_{15} correspond to the angular scales in the sky, approximately from 0.5^o to 30^0.

Since the maps have been masked by the Kp0, the wavelet coefficients localized near and within the area of the mask are affected from the zero value of the mask. This results from the convolution with the wavelets whose support overlaps the mask. To solve this problem, we extend the mask, after SMHW convolution, to exclude the wavelet coefficients strongly contaminated by the mask. The extended mask should depend on the scales R since the region covered by the support of a convolving wavelet grows with R. In other words, the number of the strongly contaminated wavelet coefficients are larger in large wavelet scale R. According to V04, the extended mask $M(R)$ for the scale R is defined to cover all pixels closer than $2.5R$ to any pixel of the mask in Galactic plane, within $|b| < 25^o$.[4] Recall that the Kp0 mask covers the regions of the Galactic foreground in Galactic plane and the radio point sources. The mask is not extended around point sources outside this region, because they contaminate only a small minority of wavelet coefficients on small scales and their effects get averaged out on larger scales. The extension around point sources also causes too few surviving wavelet coefficients for statistical analysis, i.e. V04 concluded that this definition of extended mask $M(R)$ is good enough for non-Gaussianity detections. The figures of the set of the

---

[4] b is the Galactic latitude.

extended masks $M(R)$ can be found in V04.

Because of the space-scale localization of wavelet coefficients, the non-Gaussianity investigations can be performed in several ways in the wavelet space so that the region in space-scale plane where the non-Gaussianity lives can be specified. In this section, we discuss the methods of the investigation of non-Gaussian signatures in wavelet space applied by V04 and MW04 and the results.

4.5.1 Skewness and Kurtosis of Wavelet Coefficients

The wavelet technique enables us to consider the CMB maps in each interval of scales as represented by the wavelet coefficients in the given wavelet scale. From the assumption that the CMB map is homogeneous and isotropic, we can perform the Gaussianity test by considering one-point distribution in each wavelet scale R. Hence, we can characterize the deviations from Gaussian statistics by using the skewness $S(R)$ (the third moment on scale R) and kurtosis $K(R)$ (the forth moment on scale R) according to V04:

$$S(R) = \frac{1}{N_R} \sum_{i=1}^{N_R} \frac{{w_i}^3(R)}{\sigma^3(R)}, \qquad (4.11)$$

$$K(R) = \frac{1}{N_R} \sum_{i=1}^{N_R} \frac{{w_i}^4(R)}{\sigma^4(R)} - 3, \qquad (4.12)$$

where N_R is the number of coefficients at scale R and $\sigma(R)$ is the dispersion of coefficients at scale R where

$$\sigma^2(R) = \frac{1}{N_R} \sum_{i=1}^{N_R} {w_i}^2(R) \qquad (4.13)$$

The results on all sky data

The skewness and kurtosis on each scale R were determined on the all sky data in V04 as shown in Fig. 4.4. From the figure, the values of the kurtosis spectra $K(R)$ at $R_8 = 4.17^o$ and $R_9 = 5^o$ are outside the acceptance interval at the 1% significance level, while all others, including the skewness spectra on all scales and the kurtosis spectra on other scales, are within the acceptance interval at the

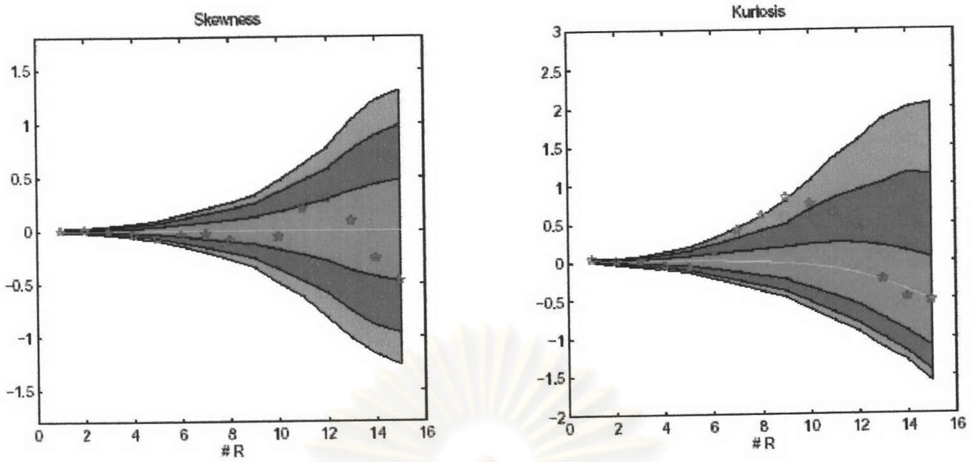

Figure 4.4: The skewness spectra $S(R)$ (left panel) and kurtosis spectra $K(R)$ (right panel) of *all sky* WMAP data determined from the wavelet coefficients at the scale R outside the extended mask $M(R)$ (blue stars). From 10000 Gaussian simulations, the red (inner), green (middle), and magenta (outer) show the acceptance intervals for the 32%, 5% , and 1% significance levels, and the yellow line represent the mean value of all simulations. This figure is taken from V04 [27].

1% significance level. This is likely a detection of non-Gaussian signature which appears as the kurtosis around the wavelet scale $R = 4^o - 5^o$. In V04, they claim that only 40 of the 10000 simulations have a kurtosis value larger than or equal to the kurtosis value detected on the WMAP data at R_8, and the same for R_9. This corresponds to a right tail probability of $\approx 0.4\%$ for either of the two scales.

The results on northern and southern hemispheres

Along with the space-scale localization, we can consider the one-point distribution in each hemisphere, north or south, of the CMB map separately in order to prove whether the non-Gaussian signatures are distributed over all sky or they are located in a region. The skewness and kurtosis spectra determined in the northern and southern hemispheres are shown in Fig. 4.5. This figure shows us that the kurtosis, as a non-Gaussian signal, is located in the southern hemisphere. The values of the kurtosis at the $R_7 = 3.33^o$ and $R_8 = 4.17^o$ in the southern hemisphere are outside the acceptance interval at the 1% significance level. In addition, the number of simulations that present values of the kurtosis equal or larger than the one detected corresponds to a right tail probability of $\approx 0.1\%$ (only 11 of the 10000 simulations) at the $R_7 = 3.33^o$ and $\approx 0.2\%$ at the $R_8 = 4.17^o$. Therefore, we can conclude from the results of V04 that the kurtosis found around the wavelet scale $R \approx 4^o$, which corresponds to the size in the sky of around 10^o, in the all sky data is in fact located in the southern hemisphere. In particular, the specification of the region that the non-Gaussianity lives illustrate an advantage of the wavelet technique.

4.5.2 The Extremum Analysis

The extremum analysis is another method that has been used to characterize the Gaussian statistics of random field. The considerations in wavelet space enables the extremum analysis to be performed in each wavelet scale. In addition to V04, MW04 use the extremum analysis of the field of wavelet coefficients to characterize the non-Gaussian signature in the southern Galactic hemisphere. The results is shown in Fig. 4.6. In the top panel, the minima, maxima and the *rms* dispersion of the wavelet coefficients in each scale are shown. The middle and bottom panels show the number of wavelet coefficients that are larger than (mean+1σ), (mean+2σ) and (mean+3σ) and smaller than (mean-1σ), (mean-2σ) and (mean-3σ), respectively. Recall that these are considered in the southern hemisphere. We can see from the figure that the minima on the scales $R_8 = 4.17^o$ and $R_9 = 5^o$ are significant around 1%, and the number of wavelet coefficients that are smaller than (mean-3σ) at $R_6 = 2.5^o$, $R_7 = 3.33^o$, $R_8 = 4.17^o$, and $R_9 = 5^o$ are very significant outside the 99.73% acceptance interval. This is a strong detection of the deviation from Gaussian statistics. From their Gaussian realizations, there are only 3 of 1000 Gaussian realizations whose value of this estimator in *any* 4 scales is larger than the 99% acceptance interval. Therefore the number of cold pixels is too large on the scales $3 - 4^o$. MW04 pointed out that there is more than one cold spot on the scales R_6 and R_7 and mainly one cold spot on larger scales near ($b = -57^o$, $l = 209^o$) (this was pointed before by V04) contributing to this number of wavelet coefficients on the scales R_6 and R_7.[5]

---

[5] b and l are the Galactic latitude and longitude, respectively.

4.5.3 Scale-Scale Correlations

As discussed in chapter 2, we can have a Gaussian perturbation field if there is no coupling between the Fourier modes, i.e. the scales of perturbations. Hence, the scale-scale correlation can be an indicator of the presence of non-Gaussianity in CMB, as introduced in Pando et al. [21]. MW04 determined this estimator in their works by defining the scale-scale correlation, the correlation between the scales R_i and R_j, as

$$C_{R_i,R_j} = \frac{N \sum_{\mathbf{x}} w^2(R_i,\mathbf{x}) w^2(R_j,\mathbf{x})}{\sum_{\mathbf{x}} w^2(R_i,\mathbf{x}) \sum_{\mathbf{x}} w^2(R_j,\mathbf{x})}, \tag{4.14}$$

where $w(R_i, \mathbf{x})$ are the wavelet coefficients on scale R_i and the position $\mathbf{x}$ in the sky, and N is the number of unmasked coefficients on the larger scale among the two scales. By calculating the scale-scale correlations of the WMAP data and the Gaussian simulations, they show the results in Fig. 4.7. The scale-scale correlations calculated from the all-sky unmasked data is consistent with being Gaussian as shown in the top panel, i.e. there is no strong signal that the scale-scale correlations are outside the acceptance interval. However, the scale-scale correlations in the southern Galactic hemisphere indicate a non-Gaussian detection as shown in the bottom panel where the scale-scale correlations amongst wavelet coefficients between the scales R_6 to R_{10}, the range of scales within which the excess kurtosis and the too large number of cold wavelet coefficients appear. In the bottom panel, many pairs of wavelet scales have correlations that are outside the acceptance interval at the 0.3% significance level (bounded by the 3σ confidence contour).

4.6 f_{NL} constraints

So far, we have described the detections of non-Gaussianity using wavelet-based method and found that the results are likely positive. If there exists *really* the non-Gaussianity, what would its origin be? It will be interesting if its origin is in part contributed by the processes in the early universe. As discussed in chapter 2, the degree of the primordial non-Gaussianity allowed by the data may help discriminate between the models of inflation. This is an important aim of the detection of non-Gaussianity. Although there are many ways to deviate from Gaussian, a phenomenological way of parametrizing the level of non-Gaussianity in the cosmological perturbations is to introduce the dimensionless "nonlinearity" parameter f_{NL} through Bardeen's gravitational potential[6] [15]

$$\Phi(\mathbf{x}) = \Phi_L(\mathbf{x}) + f_{NL}[\Phi_L^2(\mathbf{x}) - \langle\Phi_L^2(\mathbf{x})\rangle] \tag{4.15}$$

where $\Phi_L(\mathbf{x})$ are Gaussian linear perturbations with zero mean, i.e. $\Phi(\mathbf{x})$ is Gaussian when f_{NL} is zero. The quadratic term contributes a deviation from Gaussian statistics and f_{NL} characterizes the amplitude of the quadratic term to the curvature perturbations. The one-point probability distribution function of the CMB temperature anisotropy obtained from non-Gaussian simulations for different f_{NL} by Komatsu et al. [29] are shown in Fig. 4.8. The figure shows that the maps even with f_{NL} of order 10^3 do not show sign of strong non-Gaussianity.

The degree of non-Gaussianity parametrized by f_{NL} has been predicted in several models of inflation as summarized in Bartolo et al. [15]. Hence, the measurement of f_{NL} gives a way to compare directly the non-Gaussianity from the inflationary models with the data. Ideally, f_{NL} measured from the data will be a discriminator between the models of the early universe. However, the measurement of f_{NL} is difficult since the predicted degree of the primordial non-Gaussianity in this form is generally small, and there are other non-Gaussianity sources: the foreground contaminations, instrumental noises, many secondary sources of CMB anisotropy, contaminating this non-Gaussian signature.

What we can do is to constrain f_{NL} instead, i.e. the upper and lower bounds of f_{NL} are specified. Several statistical tests have been applied to constrain f_{NL}. For instance, the analysis based on the bispectrum, an optimal method especially to detect this form of non-Gaussianity, by Komatsu et al. 2002 [31] set $|f_{NL}| < 1500$ at 68% confidence level. Since the quadratic term which is the small part in the curvature perturbations causes asymmetry of the distribution, Cayon et al. 2003 [32] suggested that the skewness is most sensitive to this form of non-Gaussianity, rather than any higher order cumulants. Hence they combined all scales of the skewness of SMHW coefficients into the Fisher discriminant function

---

[6] Actually, it is the Bardeen's gauge-invariant variable which is widely known in the cosmological perturbation theory. It gives the analogy of the Newtonian gravitational potential.

to constrain f_{NL} and the limit of f_{NL} was placed to be $|f_{NL}| < 1100$ at 68% confidence level which is tighter than the one obtained from the bispectrum. On the WMAP 1st-year data, Komatsu et al. 2003 placed the limit of $-58 < f_{NL} < 134$ at 95% confidence level. The wavelet method was also applied to the WMAP 1st-year data to constrain f_{NL} by MW04.

To constrain f_{NL}, a large number of non-Gaussian simulations, which include noise and beam convolution of the WMAP 1st-year data in the same way as described earlier in Gaussain simulations, are produced. Since producing these maps is a computationally intensive process, MW04 suggested to use only 300 non-Gaussian simulations for a given value of f_{NL} at HEALPIX resolution $N_{side} = 256$ to calculate the mean value of skewness at each of different scales.[7] Furthermore, they use Gaussian simulations to estimate covariance matrix of the skewness values for the different scales and estimate the uncertainty in the measured f_{NL}.

4.6.1 The χ^2 test

In the χ^2 test, the data we want to test is assumed to follow an expected model with some parameters. The purpose of the test is to determine the parameters that best fit the data. In other words, the χ^2 test enables finding the values of parameters. Comparing a measurement of the data with one of the model, the best fit should be at the minimum χ^2 value. To constrain f_{NL}, we compare the skewness values of the data at 15 scales with those of simulations by using the generalized χ^2:

$$\chi^2 = \sum_{R_i,R_j} \left[S(R_i) - \bar{S}_{sim}(R_i)\right] \Sigma^{-1}_{R_i,R_j} \left[S(R_j) - \bar{S}_{sim}(R_j)\right], \tag{4.16}$$

where $S(R_i)$ is the skewness of the WMAP data on the ith scale R_i, $\bar{S}_{sim}$ is the mean value of the skewness at the ith scale from Monte Carlo simulations for a given value of f_{NL}, and Σ_{R_i,R_j} represents the covariance matrix between the

---

[7] The production of non-Gaussian simulations with f_{NL} are described in detail in the Appexdix of Komatsu et al. [29] and the faster method of the production of the maps are described in Liguori et al. [33].

skewness at different scales from simulations defined by

$$\Sigma_{R_i,R_j} \equiv \langle (S_{R_i} - \langle S_{R_i}\rangle)(S_{R_j} - \langle S_{R_j}\rangle)\rangle$$
$$= \langle S(R_i)S(R_j)\rangle - \langle S(R_i)\rangle\langle S(R_j)\rangle; \qquad (4.17)$$

$\langle\cdot\rangle$ denotes ensemble average which can be replaced by the average over all simulations. Notice that if there is no correlation between the skewness at different scales, the covariance matrix is diagonal and, consequently, χ^2 in Eq. (4.16) becomes the χ^2 in the standard form.

MW04 performed the χ^2 tests on simulated maps to ensure that the χ^2 statistics accurately recovers f_{NL}. The 300 non-Gaussian simulations with f_{NL} values of 50, 100 and 150 were produced and then the χ^2 was calculated for each map following Eq. (4.16). Note that we obtain the χ^2 value of a map for each $\bar{S}_{sim}$ calculated with each value of f_{NL}. Thus, we have a curve of χ^2 against f_{NL} for each map. More precisely, 300 curves of χ^2 against f_{NL} are obtained for each of values of $f_{NL} = 50, 100$ and 150. Therefore, the curves of the mean χ^2 calculated from 300 curves for each value of $f_{NL} = 50, 100$ and 150 are obtained as shown in Fig. 4.9. The figure shows that the χ^2 curves have the minimum at the f_{NL} values that was set in simulations. This means that each curve provides the accurate value of f_{NL}, as the minimum.

A curve of χ^2 against f_{NL} obtained from the data is shown in Fig. 4.10. f_{NL} is thus constrained to be 50 ± 80 at 68% confidence level, and less than 220 and 280 at 95% and 99% confidence levels, respectively.

4.6.2 The Fisher Discriminant Function

Suppose that the results of a measurement is multicomponent described by $\mathbf{x} = (x_1, \ldots, x_n)$, we want to examine which models the measured values follow between H_0, usually called the null hypothesis, and an alternative hypothesis H_1. For our case, H_0 represents the skewness spectra drawn from a Gaussian model and H_1 the skewness spectra drawn from a non-Gaussian model parametrized by f_{NL}. The joint probabilities of H_0 and H_1 to obtain the particular values of the measurement are given by $f(\mathbf{x}|H_0)$ and $f(\mathbf{x}|H_1)$, respectively. According to Neyman-Pearson lemma, the optimal test statistics in the sense of maximum power for a given significance level is given by the likelihood ratio [25]

$$t(\mathbf{x}) = \frac{f(\mathbf{x}|H_0)}{f(\mathbf{x}|H_1)}. \tag{4.18}$$

Unfortunately, in order to construct this statistics, we need to know those multi-dimensional probability distribution functions which are in general not available.

A simpler way is to construct a test statistics using the Fisher discriminant function [34] [35]. It is a linear function of the measured variables that maximizes the separation between the two probability distribution functions of the test statistics t, $g(t|H_0)$ and $g(t|H_1)$. Such a separation is defined as the ratio $(\tau_0 - \tau_1)^2/(\Sigma_0^2 + \Sigma_1^2)$, where τ_k and Σ_k^2, $k = 0, 1$, are the mean and the variance of $g(t|H_k)$, respectively [25]. The Fisher discriminant function is given by

$$t(\mathbf{x}) = (\mathbf{m}_0 - \mathbf{m}_1)^T \mathbf{W}^{-1}\mathbf{x}, \tag{4.19}$$

with $\mathbf{W} = \mathbf{V}_0 + \mathbf{V}_1$, $\mathbf{V}_k$ the covariance matrix and $\mathbf{m}_k$ the mean values (expectation values) of $f(\mathbf{x}|H_k)$; $(V_k)_{ij} \equiv \int \mathrm{d}\mathbf{x}\,(x - m_k)_i(x - m_k)_j f(\mathbf{x}|H_k)$ and $(m_k)_i \equiv \int \mathrm{d}\mathbf{x}\, x_i f(\mathbf{x}|H_k)$ where $k = 0, 1$ (hypothesis) and $i, j = 1, \ldots, n$ (component of $\mathbf{x}$).

Using the Fisher discriminant to constrain f_{NL}, the skewness values on the 15 scales: $S(R_i); i = 1, \ldots, 15$, are the components of $\mathbf{x}$, the subscript 0 is for the Gaussian case and the subscript 1 for the map that we consider. The Fisher discriminant function is calculated for the Gaussian realization, non-Gaussian realization with different f_{NL} and the data. The mean values contained in m_k, $k = 0, 1$ and covariance matrices $\mathbf{V}_k$, $k = 0, 1$ of the skewness at each wavelet scale for the Gaussian and non-Gaussian models are obtained from a large number of simulations.

We can therefore estimate the probability that the data are drawn from one or the other hypothesis: Gaussian and non-Gaussian cases. Fig. 4.11 shows the histograms of 1000 Gaussian realizations (solid), of 300 non-Gaussian realizations (dashed), and of the data (vertical line). This form of diagram enables us to place the limits of f_{NL} at a desirable significance level. The distribution of the Fisher discriminant function t (dashed) of the non-Gaussian realizations shifts to the right (more positive) as f_{NL} increases (when f_{NL} is positive), while the distribution of t of the Gaussian simulations stays around zero and the value of t of the data is quite unchanged. The figure shows the histograms at $f_{NL} = 120$ and 250; these values are close to the 1σ and 2σ limit, 74% and 95% of the non-Gaussian simulations have larger values of the Fisher discriminant than the data. This means that f_{NL} is constrained to be less than 120 and 250 at 1σ and 2σ significance level, respectively.

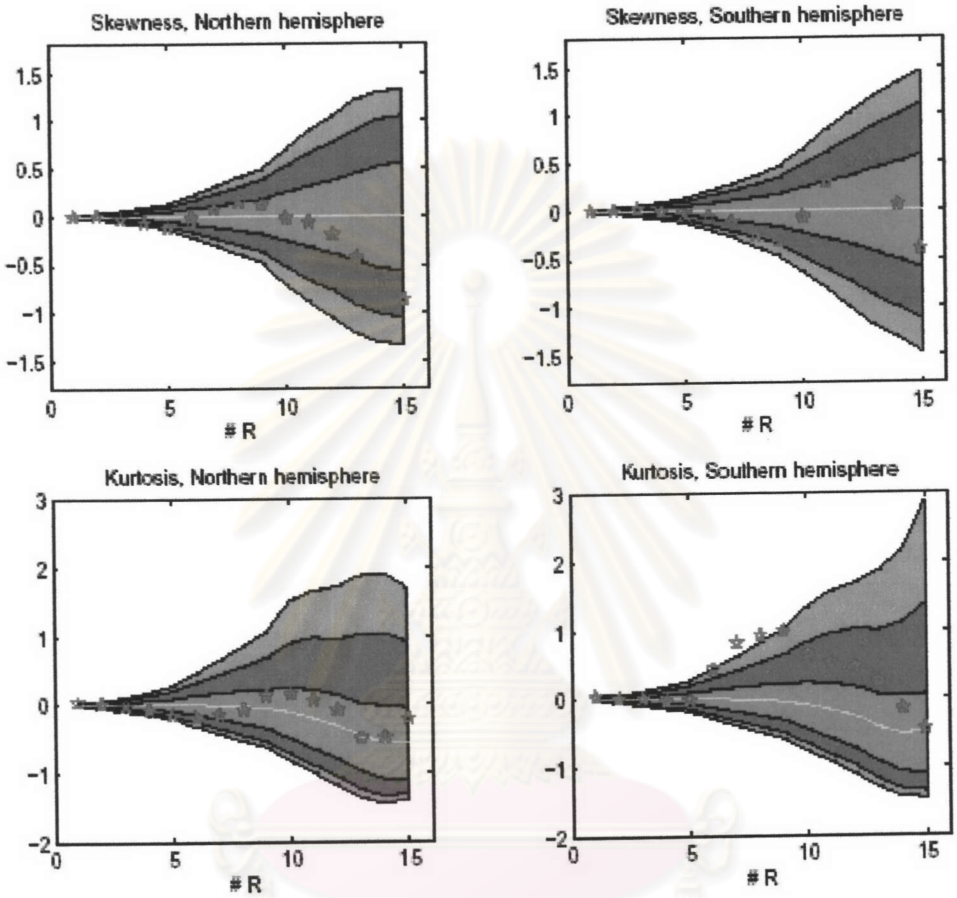

Figure 4.5: The skewness spectra $S(R)$ (top) and kurtosis spectra $K(R)$ (bottom) determined in the northern hemisphere (left column) and in the southern hemisphere (right column) of the WMAP coadded data (blue stars). From 10000 Gaussian simulations, the red (inner), green (middle), and magenta (outer) show the acceptance intervals for the 32 %, 5 % , and 1 % significance levels, and the yellow line represent the mean value of all simulations. This figure is taken from V04 [27].

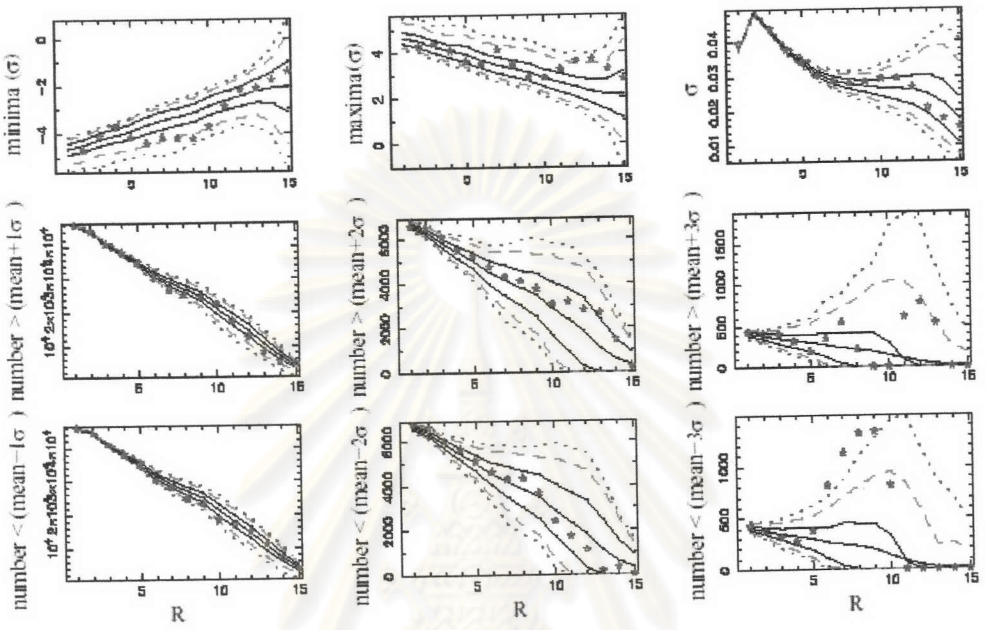

Figure 4.6: The extremum statistics of wavelet coefficients in the southern Galactic hemisphere: the minima and maxima, in unit of the dispersion σ, and σ itself (top panel), and the number of wavelet coefficients that are larger than (mean+σ), (mean+2σ) and (mean+3σ) (middle panel), and smaller than (mean-σ), (mean-2σ) and (mean-3σ) (bottom panel) measured on the WMAP coadded data, together with the mean (solid), 1σ (covering 68.27% acceptance interval) (solid), 2σ (covering 95.45% acceptance interval)(dashed), 3σ (covering 99.73% acceptance interval)(dotted) confidence contours obtained from 1000 Gaussian simulations. The panels of the minima (top-left) and the number of the coefficients less than (mean-3σ) (bottom-right) infer an excess of cold coefficients. This figure is taken from MW04 [28].

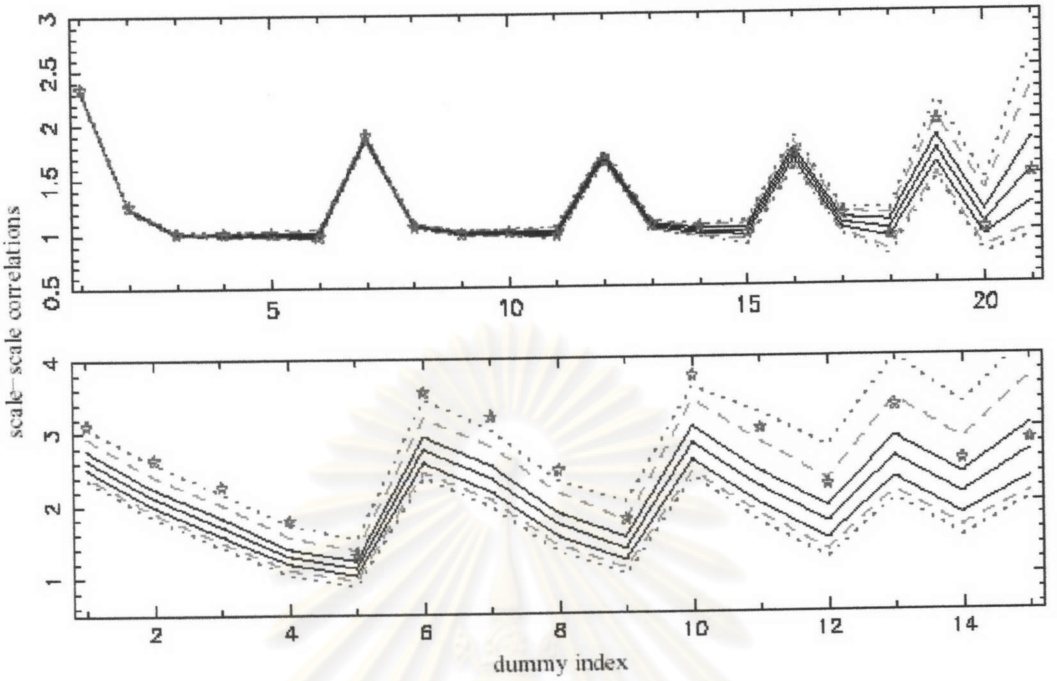

index#	1	2	3	4	5	6	7	8
top panel	R_1,R_2	R_1,R_1	R_1,R_5	R_1,R_7	R_1,R_{10}	R_1,R_{14}	R_2,R_3	R_2,R_5
index#	9	10	11	12	13	14	15	16
top panel	R_2,R_7	R_2,R_{10}	R_2,R_{14}	R_3,R_5	R_3,R_7	R_3,R_{10}	R_3,R_{14}	R_5,R_7
index#	17	18	19	20	21			
top panel	R_5,R_{10}	R_5,R_{14}	R_7,R_{10}	R_7,R_{14}	R_{10},R_{14}			
index#	1	2	3	4	5	6	7	8
bottom panel	R_6,R_7	R_6,R_8	R_6,R_9	R_6,R_{10}	R_6,R_{11}	R_7,R_8	R_7,R_9	R_7,R_{10}
index#	9	10	11	12	13	14	15	
bottom panel	R_7,R_{11}	R_8,R_9	R_8,R_{10}	R_8,R_{11}	R_9,R_{10}	R_9,R_{11}	R_{10},R_{11}	

Figure 4.7: The scale-scale correlations amongst wavelet coefficients between scales indicated in the table for the all sky data (top panel) and the data of the southern Galactic hemisphere (bottom panel) (both presented as stars). Notice that the scales considered for the southern hemisphere concentrate on the scales R_6 to R_{11} which are the scales that present non-Gaussian signals in two previous sections. The mean and 1σ (solid), 2σ (dashed) and 3σ (dotted) confidence contours obtained from Gaussian simulations are also shown [28].

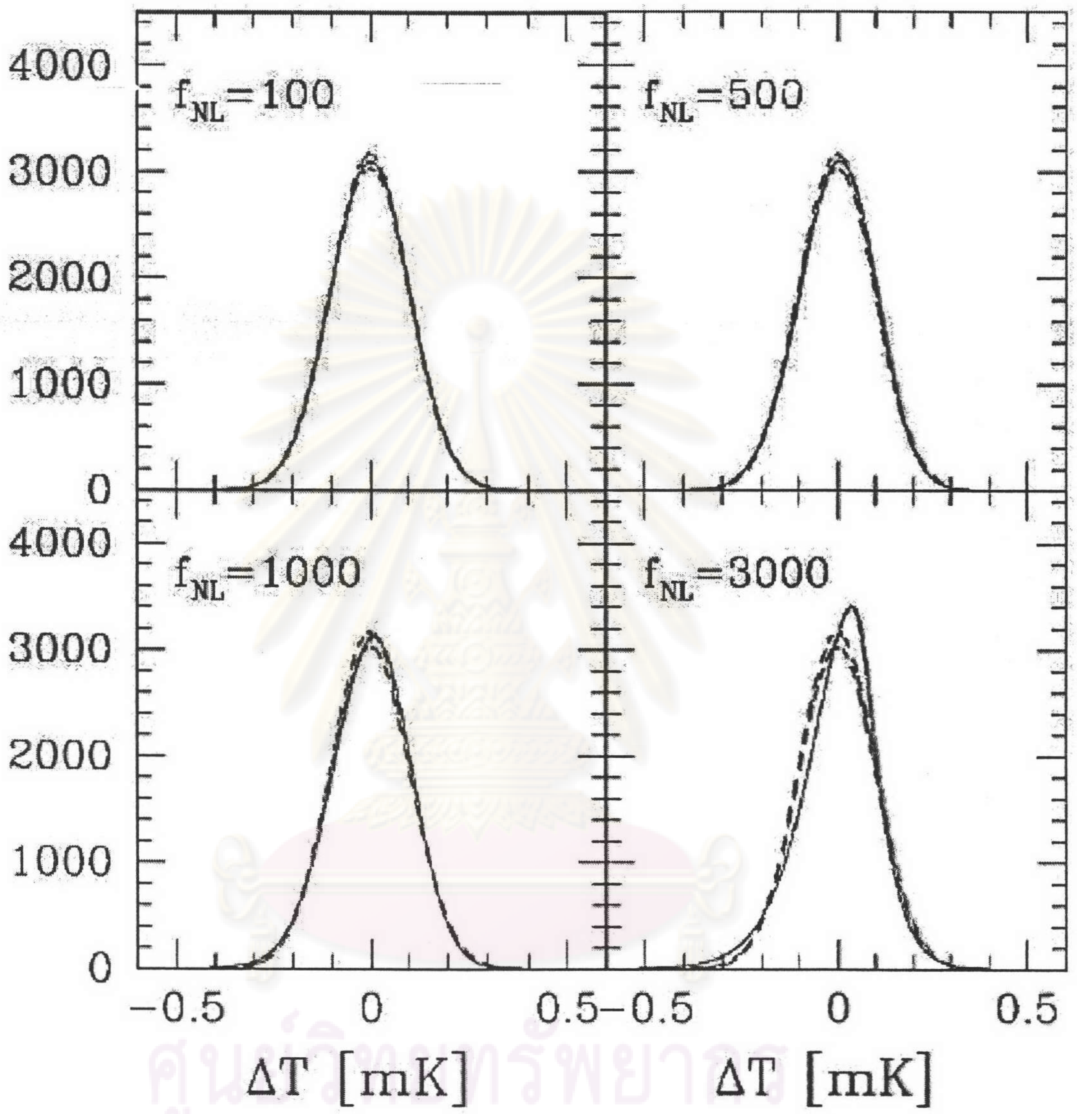

Figure 4.8: One-point probability distribution function (p.d.f.) of the CMB anisotropy, $\Delta T/T$, measured from simulated non-Gaussian maps (noise and beam smearing are not included) for $f_{NL} = 100, 500, 1000$ and 3000 (solid line). The dashed line enclose the rms scatter of Gaussian realization (i.e., $f_{NL} = 0$). Notice that the larger f_{NL} is, the more negatively skewed p.d.f. becomes. If $f_{NL} < 0$, p.d.f. becomes positively skewed [29].

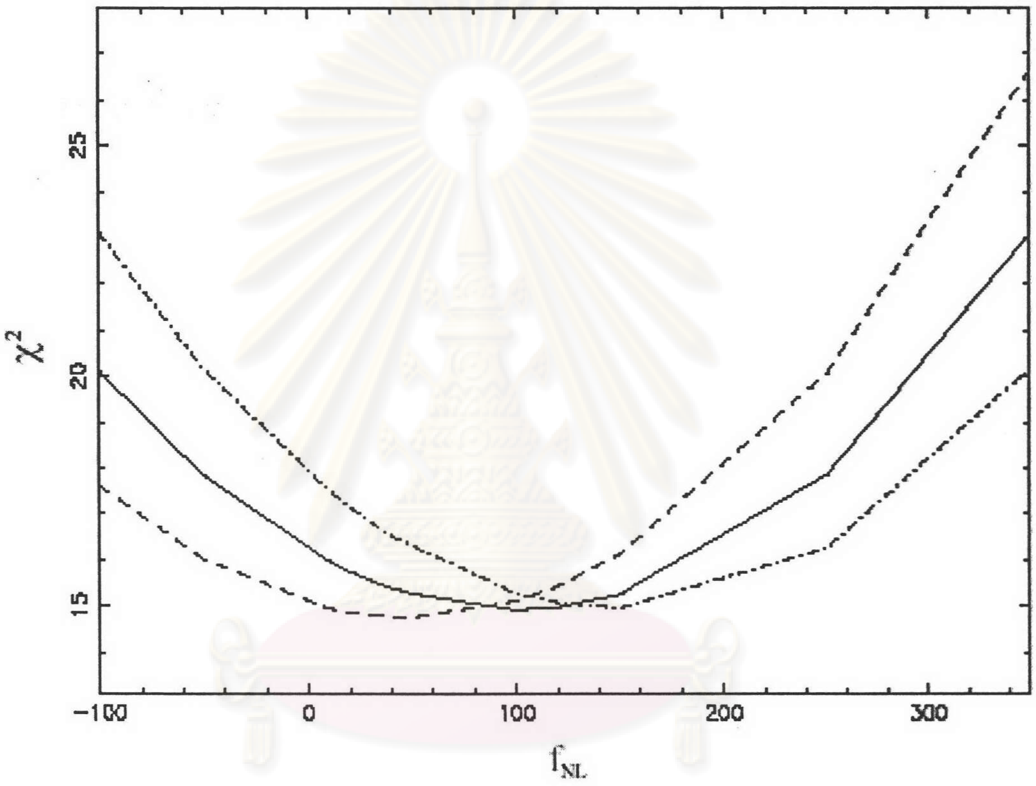

Figure 4.9: Mean χ^2 distributions obtained from 300 simulations of non-Gaussian simulations with f_{NL} values of 50 (dashed), 100 (solid), 150 (dot-dashed). The simulations include as usual the noise properties and beam convolutions of the WMAP 1st-year data. This figure is obtained from MW04 [28].

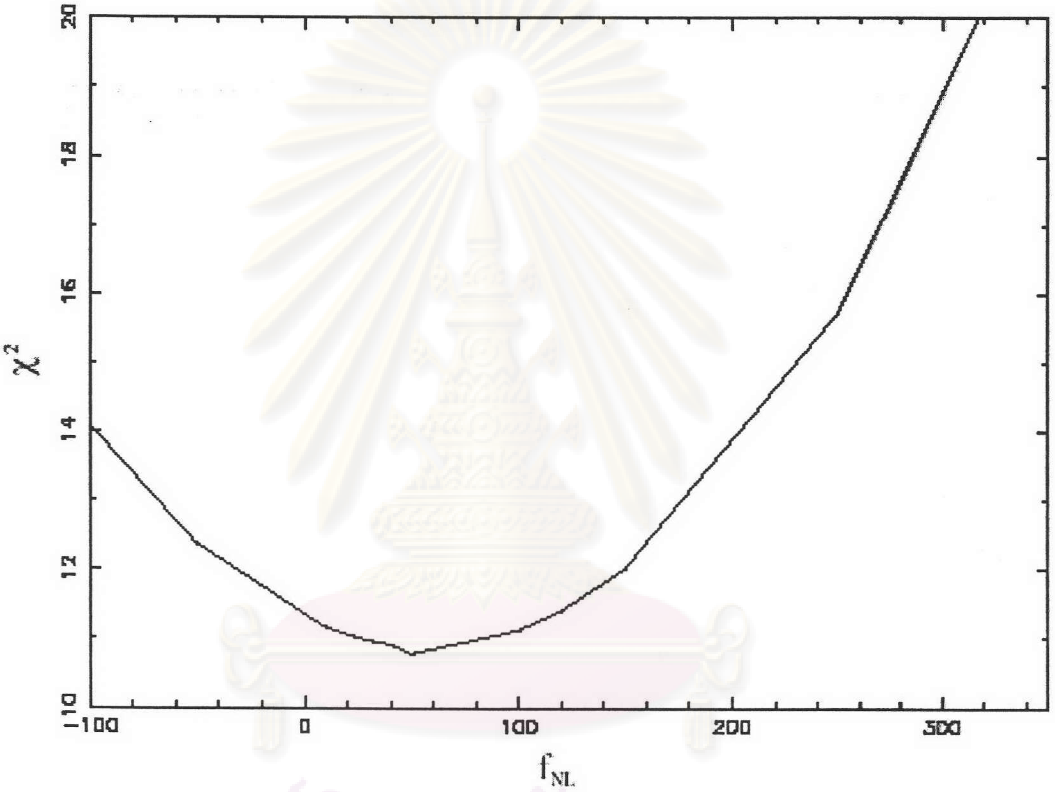

Figure 4.10: A plot of χ^2 against f_{NL} obtained using WMAP data. f_{NL} is thus estimated to be 50 ± 80 at 68% confidence, and the 95% and 99% upper limits are 220 and 280 respectively. This figure is taken from MW04 [28].

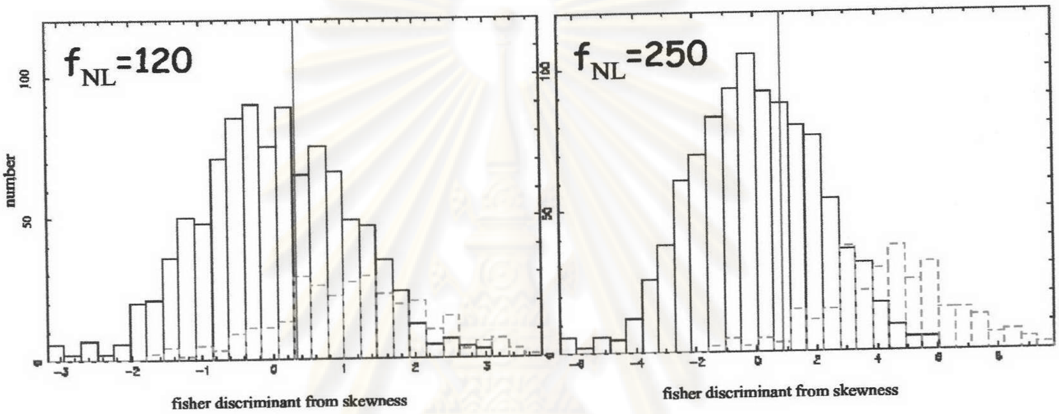

Figure 4.11: Histograms of Fisher discriminant values from 1000 Gaussian simulations (solid), from 300 non-Gaussian simulations (dashed), and of the data (vertical line), for $f_{NL} = 120$ and 250. These values are near the 1σ and 2σ limits on f_{NL}. This figure is taken from MW04 [28].